Geochemistry, Geophysics, Geosystems®

RESEARCH ARTICLE
10.1029/2022GC010769

Key Points:

- Mass-independent fraction of Hg isotopes is observed in Mesozoic gold deposits in the northern margin of the North China Craton
- Positive Δ^{199}Hg values in Mesozoic gold deposits suggest Hg was sourced from lithospheric mantle modified by oceanic subduction
- Negative Δ^{199}Hg values in Mesozoic gold deposits suggest that Hg was sourced from the Precambrian basement

Correspondence to:
R. Yin,
yinrunsheng@mail.gyig.ac.cn

Citation:
Xiao, T., Sun, D., Lehmann, B., Tian, Z., Gao, L., Zhang, D., et al. (2023). Paleo-Pacific plate subduction and basement mobilization triggered large-scale formation of Mesozoic gold deposits in the northern margin of the North China Craton. *Geochemistry, Geophysics, Geosystems*, *24*, e2022GC010769. https://doi.org/10.1029/2022GC010769

Received 1 NOV 2022
Accepted 16 JUN 2023

Paleo-Pacific Plate Subduction and Basement Mobilization Triggered Large-Scale Formation of Mesozoic Gold Deposits in the Northern Margin of the North China Craton

Tingting Xiao[1,2], Deyou Sun[1], Bernd Lehmann[3], Zhendong Tian[2], Lingjian Gao[1,2], Duo Zhang[1], Changzhou Deng[2], Anbo Luo[2], Yang Xu[2], and Runsheng Yin[1,2]

[1]College of Earth Sciences, Jilin University, Changchun, China, [2]State Key Laboratory of Ore Deposit Geochemistry, Institute of Geochemistry, Chinese Academy of Sciences, Guiyang, China, [3]Mineral Resources, Technical University of Clausthal, Clausthal-Zellerfeld, Germany

Abstract The northern margin of the North China Craton (NNCC) hosts Mesozoic gold deposits of significant economic importance. The metal sources of these gold systems have long been debated with mainly magmatic-hydrothermal versus metamorphic fluid models. Mercury (Hg) isotopes, which undergo unique mass-independent fractionation, can provide important insights into the source of metals in gold deposits due to the close association between Hg and Au in such systems. Here, we investigated the Hg isotopic composition of six gold deposits of the Middle Jurassic to Early Cretaceous age and potential source rocks in the NNCC. Variable Δ^{199}Hg values were observed in bulk ore and pyrite samples (−0.28‰ to 0.34‰, $n = 51$) and coeval granites (−0.21‰ to 0.13‰; $n = 25$). The negative Δ^{199}Hg values of bulk ore and pyrite samples mostly agree with that observed for metamorphic basement rocks (−0.37‰ to 0.11‰; $n = 32$). The positive Δ^{199}Hg values of bulk ore and pyrite samples agree with those reported in marine sediments (0‰–0.3‰). So the data suggest binary mixing of ocean-recycled Hg originated from the subducted oceanic slab, and terrestrial-recycled Hg from the Precambrian basement in Mesozoic gold deposits. The contribution of Hg (and Au, by analogy) from both reservoirs varies depending on active continental arc versus intracontinental setting and is ultimately controlled by translithospheric heat flow driven by paleo-Pacific plate subduction.

Plain Language Summary Photoreduction of Hg(II) on Earth's surface system leads to mass-independent fractionation of Hg isotopes, resulting in positive and negative Δ^{199}Hg values in marine and terrestrial systems, respectively. Here, we observe negative to positive Δ^{199}Hg values in the Mesozoic gold deposits in the northern margin of the North China Craton. These results suggest binary mixing of ocean-recycled Hg from the fluids released by subducting oceanic slab or the mantle metasomatized by these fluids, and terrestrial-recycled Hg from the Precambrian basement in Mesozoic gold deposits. Paleo-Pacific plate subduction and translithospheric heat flow may have played a key role in the metallogenic metal enrichment of the Mesozoic gold deposits in the northern margin of the North China Craton.

1. Introduction

In the Mesozoic, subduction of the paleo-Pacific plate beneath the North China Craton (NCC) led to delamination and destruction of the NCC (S. H. Zhang et al., 2014; Zhu & Sun., 2021), widespread magmatism, and hydrothermal gold formation in the northern margin of the North China Craton (NNCC, Li et al., 2012; N'dri et al., 2021; Yang et al., 2003, 2008). Subduction of the paleo-Pacific plate caused lithospheric thinning and upwelling of the asthenosphere, forming widespread Middle Jurassic to Early Cretaceous granites (Yang et al., 2008; S. H. Zhang et al., 2014). The coeval gold deposits contain a total resource of >1,000 tonnes Au; however, their genesis remains unclear. Some studies have suggested that the ore-forming metals are of magmatic-hydrothermal origin (e.g., N'dri et al., 2021; Yang et al., 2021), while others classify these deposits as orogenic gold deposits in which the ore-forming metals could be sourced from the Precambrian metamorphic basement or sediments on the top of the subducting slab (Goldfarb & Pitcairn, 2022; Goldfarb et al., 2001, 2019; Tomkins, 2010). According to Goldschmidt's geochemical classification of elements, Hg and Au belong to chalcophile elements and share similar geochemical behavior during hydrothermal processes. As a result, Hg is a common component enriched in hydrothermal gold deposits. Recent studies on Hg isotopes in hydrothermal gold deposits have provided important insights into the source of gold, given that Hg isotopes (^{196}Hg, $^{198–202}$Hg, ^{204}Hg) undergo

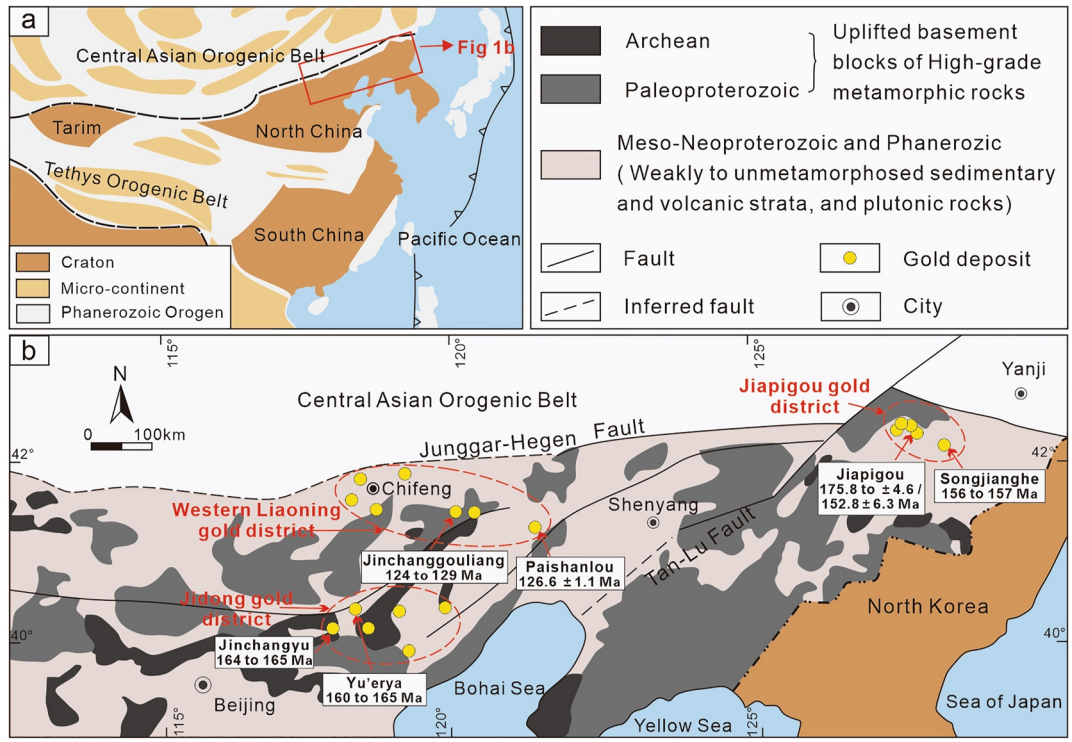

Figure 1. Regional geological map of the northern North China Craton (after N'dri et al. (2021)) with age data for gold deposits studied here.

mass-dependent fractionation (MDF, expressed as δ^{202}Hg) and unique mass-independent fractionation (MIF, expressed as Δ^{199}Hg). A variety of biological, chemical, and physical processes can trigger Hg-MDF (Blum et al., 2014); however, Hg-MIF mainly occurs during photochemical reactions with limited interference from other processes (Bergquist & Blum, 2007). Magmatic, metamorphic, and hydrothermal processes do not induce Hg-MIF, allowing the use of Hg-MIF signals for tracing metal sources in geological reservoirs (Chen et al., 2022; Deng et al., 2021; Deng, Hong, et al., 2022; Tian et al., 2022; Yin et al., 2022). The primitive mantle has near-zero Δ^{199}Hg values (0.00‰ ± 0.10‰, Moynier et al., 2021), whereas photochemical processes on Earth's surface result in negative and positive Δ^{199}Hg values in terrestrial (soil and vegetation) and oceanic (seawater and marine sediments) reservoirs, respectively (Blum et al., 2014). The recent observation of positive Δ^{199}Hg values in global basalts and arc-related epithermal gold systems at convergent plate margins highlight marine Hg recycling into the mantle and crust via oceanic plate subduction (Deng et al., 2021; Moynier et al., 2021; Yin et al., 2022). The observation of negative Δ^{199}Hg values in intracontinental epithermal gold deposits in south China and NE China (Deng, Lehmann, et al., 2022) suggests terrestrial-derived Hg was sourced from the Precambrian metamorphic basement.

Here, we present Hg isotope data for gold ore samples collected from six Mesozoic hydrothermal gold deposits in the NNCC. Combined with analyses of potential source rocks for these gold deposits (e.g., Precambrian basement rocks, Mesozoic granites). This study aims to gain an understanding of the genesis of these Mesozoic gold systems from the perspective of Hg isotope geochemistry.

2. Geological Background

The NNCC is separated from the Central Asian Orogenic Belt by the regional-scale Junggar-Hegen fault system (Figure 1). In the NNCC, the basement consists mainly of Archean high-grade metamorphic rocks and middle- to low-grade metamorphic granite-greenstone belts, with Paleoproterozoic metamorphic volcano-sedimentary cover sequences to the Archean units (Zhao & Zhai, 2013). Meso-Neoproterozoic marine strata, Paleozoic alternating marine-terrestrial strata, Mesozoic terrestrial strata, and Quaternary sediments are exposed. Some paleozoic (N'dri et al., 2021; X. H. Zhang & Zhai, 2010; Figure 2) and abundant Mesozoic granites are distributed

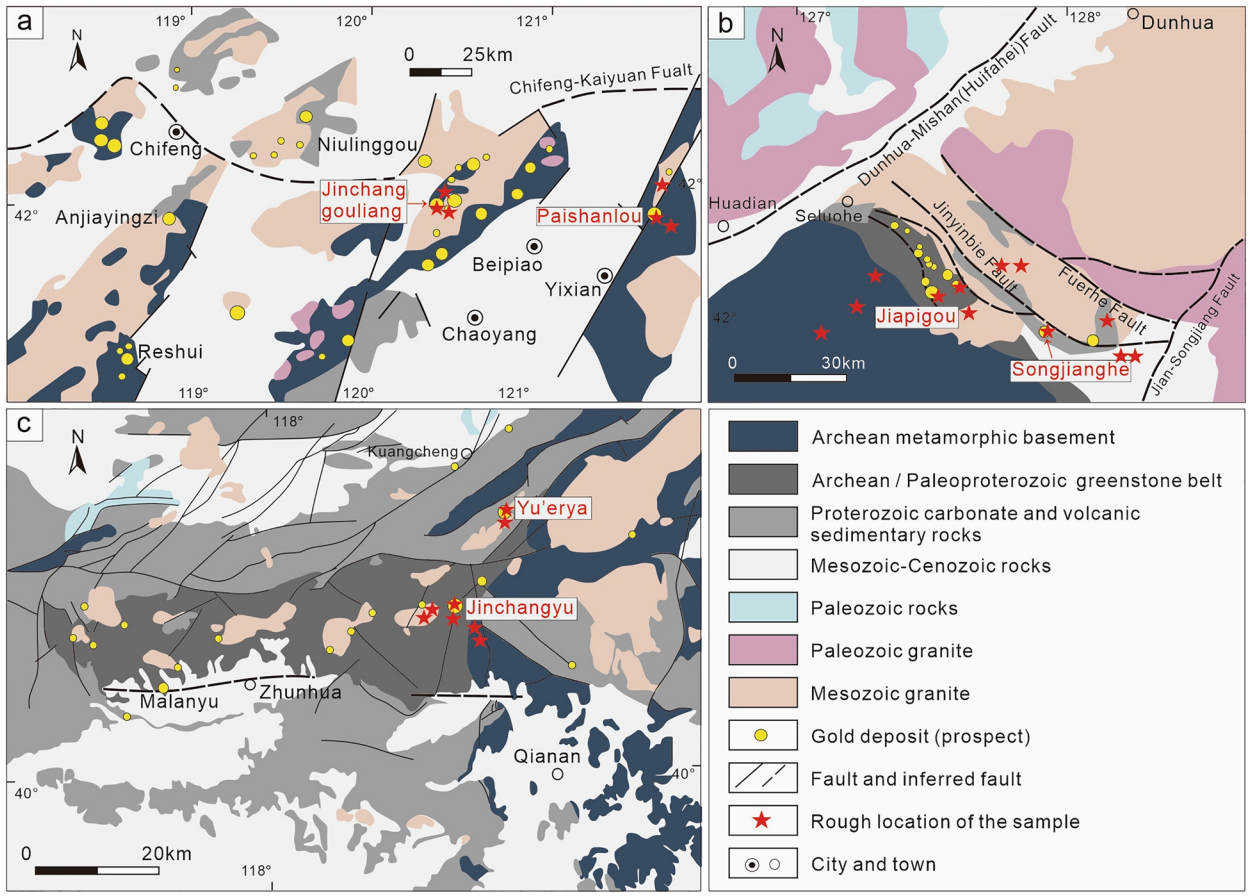

Figure 2. Regional geological map of the Mesozoic gold deposits in the northern North China Craton (after Yang et al. (2003), and Song et al. (2016)). (a) Jinchanggouliang and Paishanlou gold deposits in the Western Liaoning district; (b) Jiapigou and Songjianghe gold deposits in the Jiapigou district; and (c) Jinchangyu and Yu'erya gold deposits in the Jidong district.

throughout the area (S. H. Zhang et al., 2014; Figure 2). The Mesozoic granites are mainly emplaced into the Precambrian basement (Fu et al., 2012; Han et al., 2022; Kang et al., 1998; Lu et al., 2019; Song, 2011; S. K. Sun et al., 2012).

Mesozoic gold deposits in the NNCC were formed during two major metallogenic stages (Table 1): Middle Jurassic (e.g., Songjianghe, Jiapigou, Yu'erya and Jinchangyu deposits) and Early Cretaceous (e.g., Paishanlou and Jinchanggouliang deposits). These gold deposits are located in brittle-ductile shear zones and fractures (Figure 2). Gold occurs as disseminated or quartz veins within either the Precambrian metamorphic basement (e.g., Songjianghe, Jiapigou, Paishanlou, Jinchanggouliang, and Jinchangyu; L. Liu et al., 2020; S. F. Liu et al., 2021; Song et al., 2016; X. H. Zhang et al., 2005; X. T. Zhang et al., 2019) or Mesozoic granites (e.g., Yu'erya; Kong et al., 2015). The sulfides in the ore include pyrite, chalcopyrite, galena, and sphalerite. Pyrite is the major gold-bearing mineral. Fluid inclusion studies indicate that the ore-forming fluids belong to the H_2O-NaCl-CO_2-CH_4 system, with low to intermediate salinity (1.1–15.3 wt.% NaCl eq.) and temperatures in the range of ~200–~400°C (Table 1 and references therein). A total of 51 ore samples were collected from the above-mentioned six gold deposits in three major gold districts named Jiapigou, Western Liaoning, and Jidong (Figure 1b). The ore samples are mainly quartz vein type and disseminated altered rock type.

Potential source rocks, including Mesozoic granites (n = 25) and Precambrian basement rocks (n = 30), were also collected in the vicinity of the studied deposits (Figure 2, Tables 3 and 4). These rocks are fresh without influences of hydrothermal alteration. The collected granites can be divided into two ages: Early-Middle Jurassic (Huangniling and Wudaoliuhe granite from Songjianghe and Jiapigou, Yu'erya granite from Yu'erya, Qinshankou granite from Jinchangyu) and Early Cretaceous (Yilvshan granite from Paishanlou, Duimiangou granite from Jinchanggouliang). The age of the granite samples is broadly coeval with that of the corresponding gold deposit

Geochemistry, Geophysics, Geosystems

10.1029/2022GC010769

Table 1
Detailed Information of the Gold Deposits Studied

Deposit	Age (Ma)	Type of mineralization	Ore minerals	Temperature (°C)	Salinity (wt% $NaCl_{eq}$)	Depth (Km)	Main types of ore fluid inclusions	Reference
Songjianghe	156–157	Mylonized altered rock typeand Quartz vein type	Pyrite, pyrrhotite, chalcopyrite, sphalerite, and galena etc	260–390	1.4–6.8	6.8–8.7	Aqueous (H2O-NaCl) Aqueous-carbonic (CO2-H2O-NaCl) CO2-rich inclusions	Qin et al. (2019) and X. T. Zhang et al. (2019)
Jiapigou	151–176	Quartz vein type	Pyrite, galena, with lesser sphalerite, and chalcopyrite etc.	207–341	1.4–15.3	4.4–5.8	Aqueous (H_2O-NaCl), Aqueous-carbonic (CO_2-H_2O-NaCl) CO_2-rich inclusions	Dai et al. (2007), S. F. Liu et al. (2021), and X. T. Zhang et al. (2021)
Paishanlou	126 6 ± 1 1	Mylonized altered rock typeand Network veinlets type	Pyrite, chalcopyrite and pyrrhotite, with minor ilmenite, galena, sphalerite, chalcocite and millerite.	242–337	4.6–12.2	5.0–7.0	Aqueous (H_2O-NaCl), Aqueous-carbonic (CO_2-H_2O-NaCl), CO_2-rich inclusions, and Unfrequent aqueous-carbonic inclusions with a halite crystal.	X. H. Zhang et al. (2005)
Jinchanggouliang	124–129	Quartz vein type	Pyrite, chalcopyrite, galena, sphalerite etc.	245–382	1.1–10.8	2.2–2.5	Aqueous (H_2O-NaCl), Aqueous-carbonic (CO_2-H_2O-NaCl), CO_2-rich inclusions, and Unfrequent aqueous-carbonic inclusions with a halite crystal	Z. J. Sun et al. (2014), L. Liu et al. (2020), and Mo et al. (2021)
Yu'erya	160–176	Quartz veinand Veinlet disseminated style	Pyrite, sphalerite, galena, chalcopyrite, tellurobismuthite and bornite etc.	243–353	1.2–9.9	~2.14	Aqueous (H_2O-NaCl), Aqueous-carbonic (CO_2-H_2O-NaCl) CO_2-rich inclusions	Jia (2011), Kong et al. (2015), and B. W. Guo et al. (2017)
Jinchangyu	164–165	Quartz vein type,Quartz-albite vein type, and Stockworks type	Pyrite, galena, chalcopyrite, hematite molybdenite etc.	270–350	3.0–12.5	0.8–2.4	Aqueous (H_2O-NaCl), Aqueous-carbonic (CO_2-H_2O-NaCl), CO_2-rich inclusions and unfrequent aqueous-carbonic inclusions with a halite crystal.	Song et al. (2016) and H. Q. Wang et al. (2020)

Note. The information of Songjianghe deposit come from Qin et al. (2019) and X. T. Zhang et al. (2019); the information of Jiapigou deposits come from Dai et al. (2007), S. F. Liu et al. (2021), and X. T. Zhang et al. (2021); The information of Paishanlou deposit come from X. H. Zhang et al. (2005); The information of Jinchanggouliang deposit come from Z. J. Sun et al. (2014), L. Liu et al. (2020), and Mo et al. (2021); The information of Yu'erya deposit come from Jia (2011), Kong et al. (2015), and B. W. Guo et al. (2017); The information of Jinchangyu deposit come from Song et al. (2016) and H. Q. Wang et al. (2020).

(Tables 1 and 3). These granites intruded into the Precambrian basement (Figure 2). The collected basement rocks (granulite, gneiss, amphibolite, mica schist, andesite, and andesitic tuff) cover a time span from Archean to Mesoproterozoic (Table 4).

3. Methods

Twenty-five of the collected ore samples (n = 51) were used for bulk analyses, and the 26 remaining samples were used to select pyrite separates by handpicking under a binocular microscope. We failed to acquire enough chalcopyrite separates for analyses due to their small grain sizes and small amounts in the samples. Prior to chemical analyses, the ore samples and pyrite separates were powdered to 200 mesh size and homogenized in an agate mortar, in the same way as that used for granites (n = 25) and basement rocks (n = 30).

The samples and pyrite separates were then measured for total Hg concentration and Hg isotopic composition at the State Key Laboratory of Environmental Geochemistry, Institute of Geochemistry, Chinese Academy of Sciences, Guiyang, China, using a Lumex RA 915+ Hg analyzer and a Neptune Plus multi-collector inductively coupled plasma mass spectrometer, respectively (Yin et al., 2016). The collected samples were washed with deionized water, air-dried, crushed, ground to 200 mesh powder, and homogenized, prior to total Hg (THg) concentration and Hg isotopic composition analysis.

THg concentrations were measured by a Lumex RA 915+ Hg analyzer (Lumex Ltd. Russia), which yielded THg recoveries of 90%–110% for standard reference material GSS-4 (soil) and uncertainty of <10% for sample replicates. The Lumex RA 915+ Hg analyzer has an analytical uncertainty of ±10% (SD) during THg concentration analyses. A double-stage tube furnace coupled with 40% reverse aqua regia (HNO_3/HCl = 3/1, v/v) trapping solutions was used for Hg preconcentration (Zerkle et al., 2020). The trapping solutions were diluted to 1.0 ng/mL Hg in 10% HCl (v/v) prior to Hg isotope analysis by Neptune Plus multi-collector inductively coupled plasma mass spectrometry (Yin et al., 2016). Mercury isotope composition was reported following the convention (Bergquist & Blum, 2007). Hg-MDF is expressed in δ^{202}Hg notation in units of ‰ referenced to the NIST-3133 Hg standard (analyzed before and after each sample analysis):

$$\delta^{202}\mathrm{Hg}(‰) = \left[\left(^{202}\mathrm{Hg}/^{198}\mathrm{Hg}_{\mathrm{sample}}\right)/\left(^{202}\mathrm{Hg}/^{198}\mathrm{Hg}_{\mathrm{standard}}\right) - 1\right] \times 1000$$

Hg-MIF is reported in Δ notation, which describes the difference between the measured δ^{xxx}Hg and the theoretically predicted δ^{xxx}Hg value, in units of ‰, with xxx = 199, 200 or 201:

$$\Delta^{xxx}\mathrm{Hg} \approx \delta^{xxx}\mathrm{Hg} - \delta^{202}\mathrm{Hg} \times \beta$$

β is equal to 0.2520 for ^{199}Hg, 0.5024 for ^{200}Hg, and 0.7520 for ^{201}Hg (Bergquist & Blum, 2007).

GSS-4 soil standard reference material, which contains silicate substances and has Hg contents in the same order of magnitude as the rock samples, was prepared in the same way and measured at the same time as the samples. To ensure accurate measurement of the ore samples, we also conducted replicated analyses of NIST-3177 secondary Hg standard (diluted to 1.0 ng/mL Hg in 10% HCl (v/v)) at the same analytical session, given that the NIST-3177 standard is a digest of cinnabar collected from the Almaden Hg mine, Spain (Bergquist & Blum, 2007). The average and uncertainty of NIST-3177 (δ^{202}Hg: −0.51‰ ± 0.05‰; Δ^{199}Hg: 0.01‰ ± 0.03‰; Δ^{200}Hg: 0.00‰ ± 0.05‰; Δ^{201}Hg: 0.01‰ ± 0.03‰, 2SD, n = 11) and GSS-4 (δ^{202}Hg: −1.62‰ ± 0.14‰; Δ^{199}Hg: −0.35‰ ± 0.06‰; Δ^{200}Hg: 0.01‰ ± 0.03‰; Δ^{201}Hg: −0.34‰ ± 0.07‰, 2SD, n = 5) agrees well with previous results (δ^{202}Hg: −0.50‰ ± 0.10‰; Δ^{199}Hg: −0.01‰ ± 0.05‰; Δ^{201}Hg: −0.02‰ ± 0.07‰, 2SD, n = 11) and GSS-4 (δ^{202}Hg: −1.67‰ ± 0.14‰; Δ^{199}Hg: −0.34‰ ± 0.08‰; Δ^{201}Hg: −0.35‰ ± 0.07‰, 2SD, n = 5) (Deng et al., 2021). The largest 2SD values for NIST-3177 and GSS-4 represent the analytical uncertainties of our samples.

4. Results

Analytical results of this study are given in Tables 2–4. Despite published data of three basement rocks (Table 4), the results of gold ores and rocks are novel and not published elsewhere. In brief, Precambrian metamorphic basement and granite in the NCC show variable Hg concentrations of 0.46–23.6 and 0.50–12.1 ppb (Tables 3 and 4), with mean values of 4.18 ± 10.6 (n = 32, 2SD) and 1.83 ± 4.58 ppb (n = 25, 2SD), respectively. Gold-bearing

Table 2
Location, Description, Hg Concentration, and Isotopic Composition of Bulk Ore and Pyrite Samples in This Study

Sample ID	Description of sample	THg (ppb)	δ^{202}Hg (‰)	Δ^{199}Hg (‰)	Δ^{200}Hg (‰)	Δ^{201}Hg (‰)
Songjianghe 01	Mylonitized altered ore (containing sparse disseminated pyrite)	7.33	−2.45	0.05	0.08	−0.04
Songjianghe 02	Mylonitized altered ore (containing sparse disseminated pyrite)	13.0	−2.11	0.21	0.05	0.15
Songjianghe 03	Mylonitized altered ore (containing sparse disseminated pyrite)	43.7	−3.22	0.24	0.03	0.13
Songjianghe 04	Mylonitized altered ore (containing sparse disseminated pyrite)	34.4	−1.95	0.15	0.02	0.01
Songjianghe 05	Mylonitized altered ore (containing sparse disseminated pyrite)	25.3	−2.09	0.06	0.03	−0.11
Jiapigou 01	Pyrites selected from quartz vein ore	151	0.98	0.02	−0.03	−0.01
Jiapigou 02	Pyrites selected from quartz vein ore	114	−0.52	0.17	−0.08	0.13
Jiapigou 03	Pyrites selected from quartz vein ore	43.1	−1.53	0.10	0.02	0.01
Jiapigou 04	Pyrites selected from quartz vein ore	16.7	0.38	0.19	0.04	0.09
Jiapigou 05	Pyrites selected from quartz vein ore	13.6	0.54	0.05	−0.12	−0.05
Jiapigou 06	Pyrites selected from quartz vein ore	19.2	−1.30	0.32	0.03	0.23
Jiapigou 07	Pyrites selected from quartz vein ore	11.9	−1.41	0.31	0.02	0.15
Jiapigou 08	Pyrites selected from quartz vein ore	5.91	−0.86	0.15	0.00	0.15
Jiapigou 09	Pyrites selected from quartz vein ore	66.1	−1.40	0.22	0.02	0.19
Jiapigou 10	Quartz vein ore (containing pyrite, galena and chalcopyrite)	12.5	−1.40	0.17	0.04	0.15
Jiapigou 11	Quartz vein ore (containing pyrite)	4.30	−0.99	−0.10	−0.02	−0.15
Jiapigou 12	Quartz vein ore (containing pyrite, chalcopyrite, and magnetite)	3.10	−0.54	−0.08	−0.04	−0.08
Jiapigou 13	Quartz vein ore (containing pyrite, galena and chalcopyrite)	221	−1.85	0.34	0.01	0.18
Paishanlou 01	Mylonitized altered ore (containing disseminated pyrite)	107	−1.62	0.23	0.08	0.21
Paishanlou 02	Mylonitized altered ore (containing disseminated pyrite)	1.52	−0.19	0.24	−0.10	0.27
Paishanlou 03	Mylonitized altered ore (containing disseminated pyrite)	31.7	−0.24	−0.21	−0.01	−0.15
Paishanlou 04	Mylonitized altered ore (containing disseminated pyrite)	2.50	0.82	−0.01	−0.03	0.03
Paishanlou 05	Mylonitized altered ore (containing disseminated pyrite)	10.8	0.00	−0.01	−0.07	−0.18
Paishanlou 06	Mylonitized altered ore (containing disseminated pyrite)	6.49	−0.15	−0.15	−0.10	−0.18
Jinchanggouliang 01	Pyrites selected from quartz vein ore	21.1	0.10	0.03	0.02	0.09
Jinchanggouliang 02	Pyrites selected from quartz vein ore	111	−0.40	0.21	0.09	0.23
Jinchanggouliang 03	Pyrites selected from quartz vein ore	18.9	−0.11	0.11	0.03	0.00
Jinchanggouliang 04	Pyrites selected from quartz vein ore	1,229	−1.94	0.19	0.00	0.13
Jinchanggouliang 05	Pyrites selected from quartz vein ore	172	0.39	−0.11	−0.12	0.07
Jinchanggouliang 06	Pyrites selected from quartz vein ore	4.5	−2.21	0.02	−0.06	0.13
Jinchangyu 01	Pyrites selected from quartz vein ore	19.7	0.33	−0.16	0.00	−0.07
Jinchangyu 02	Pyrites selected from quartz vein ore	6.59	−0.65	−0.18	−0.09	−0.22
Jinchangyu 03	Pyrites selected from quartz vein ore	10.4	0.65	−0.13	−0.02	−0.09
Jinchangyu 04	Pyrites selected from quartz vein ore	11.7	0.54	0.01	−0.01	0.05
Jinchangyu 05	Pyrites selected from quartz vein ore	4.17	−0.17	−0.11	0.07	−0.02
Jinchangyu 06	Altered wall rock ore (containing disseminated pyrite)	0.89	−1.67	−0.12	−0.02	−0.08
Jinchangyu 07	Quartz vein ore mixed with albitized wall rock breccia (containing pyrite and chalcopyrite)	8.48	0.16	−0.24	0.00	−0.20
Jinchangyu 08	Quartz vein ore mixed with albitized wall rock breccia (containing pyrite and chalcopyrite)	85.3	0.26	−0.21	−0.02	−0.19
Jinchangyu 09	Albite-quartz vein ore (containing disseminated pyrite)	1.92	−0.64	0.10	0.03	0.07
Jinchangyu 10	Albite-quartz vein ore (containing disseminated pyrite)	2.68	−0.17	0.08	−0.02	0.08

Geochemistry, Geophysics, Geosystems

10.1029/2022GC010769

Table 3
Information, Hg Concentration, and Hg Isotopic Composition of Granite Samples

Sample ID	Rock type	Location	Age (Ma)	Source	THg (ppb)	δ^{202}Hg (‰)	Δ^{199}Hg (‰)	Δ^{200}Hg (‰)	Δ^{201}Hg (‰)
Wudaoliuhe 01	Monzogranite	127°36′26″, 42°45′11″	~175	Neoarchean crust	1.14	1.48	−0.07	−0.02	−0.05
Huangniling 01	Monzogranite	127°38′08″, 42°51′13″	153–169	Neoarchean crust	4.55	−0.69	0.13	−0.02	0.05
Huangniling 02	Monzogranite	20 m to the south of G02	153–169	Neoarchean crust	12.05	1.10	−0.07	−0.02	−0.11
Huangniling 03	Monzogranite	127°36′40″, 42°52′27″	153–169	Neoarchean crust	2.50	−0.71	0.08	0.01	0.05
Duimiangou 01	Granodiorite	120°18′01″, 41°57′34″	121–136	Mixed crust-mantle source	3.54	−1.36	−0.05	−0.09	0.02
Duimiangou 02	Granodiorite	120°18′44″, 41°56′50″	121–136	Mixed crust-mantle source	0.92	−0.77	−0.15	−0.12	−0.09
Yilvshan 01	Monzogranite	121°47′15″, 41°51′10″	121–128	Lower crust	1.38	−0.41	−0.11	0.03	−0.09
Yilvshan 02	Monzogranite	121°43′28″, 41°49′03″	121–128	Lower crust	0.77	0.02	−0.12	−0.09	−0.09
Yilvshan 03	Monzogranite	121°55′41″, 41°59′46″	121–128	Lower crust	1.08	−0.96	−0.09	−0.12	−0.06
Yilvshan 04	Monzogranite	121°50′49″, 41°56′54″	121–128	Lower crust	0.77	−1.19	−0.21	−0.12	−0.12
Yilvshan 05	Monzogranite	121°51′43″, 41°57′47″	121–128	Lower crust	0.62	−1.01	−0.16	−0.13	−0.06
Yilvshan 06	Monzogranite	121°46′43″, 41°52′54″	121–128	Lower crust	0.83	−1.39	−0.07	−0.04	−0.06
Yilvshan 07	Monzogranite	121°55′35″, 41°59′54″	121–128	Lower crust	0.67	−1.20	−0.08	−0.03	0.00
Yilvshan 08	Monzogranite	121°51′40″, 41°57′52″	121–128	Lower crust	0.67	−1.15	−0.02	−0.02	−0.01
Qinshankou 01	Biotite granite	118°23′31″, 40°17′37″	~199	Lower crust	0.77	−0.48	−0.13	−0.12	−0.08
Qinshankou 02	Biotite granite	118°23′13″, 40°18′59″	~199	Lower crust	2.00	−1.33	−0.04	0.00	0.07
Qinshankou 03	Biotite granite	118°23′23″, 40°17′40″	~199	Lower crust	0.50	−1.14	−0.05	−0.21	−0.06
Qinshankou 04	Biotite granite	118°23′28″, 40°18′11″	~199	Lower crust	2.17	−0.81	−0.03	0.03	0.13
Qinshankou 05	Biotite granite	118°23′22″, 40°18′15″	~199	Lower crust	1.67	−0.66	0.04	−0.06	0.08
Qinshankou 06	Biotite granite	118°23′16″, 40°18′54″	~199	Lower crust	0.50	−1.21	−0.11	−0.06	−0.13
Yu'erya 01	Biotite monzogranite	Mining area	160–176	Lower crust	1.08	−0.41	0.05	0.03	−0.08
Yu'erya 02	Biotite monzogranite	Mining area	160–176	Lower crust	1.17	−1.37	0.03	−0.11	0.04
Yu'erya 03	Biotite monzogranite	Mining area	160–176	Lower crust	2.17	−1.08	−0.17	−0.03	−0.11
Yu'erya 04	Biotite monzogranite	Mining area	160–176	Lower crust	1.33	−1.13	−0.06	0.07	0.01
Yu'erya 05	Biotite monzogranite	Mining area	160–176	Lower crust	1.83	−0.02	0.02	−0.04	−0.02

Note. The Wudaoliuhe and Huangniling granite samples were collected from the southeast of Jiapigou. The Duimiangou granite and rhyolite samples were respectively collected from the south and east of Jinchanggouliang. The Yilvshan granite samples were collected from the northeast of Paishanlou. The Qinshankou granite samples were collected from the west of Jinchangyu. The Yu'erya granite samples were collected in the mining area of Yu'erya. The age and magma source of Toudaoliuhe granite intrusion are quoted from Han et al. (2022). The age of Huangniling granite intrusion is quoted from Y. B. Zhang et al. (2002) and Lu et al. (2019), and the magma source of Huangniling granite intrusion is quoted from Lu et al. (2019). The age and magma source of Duimiangou granite intrusion are quoted from Fu et al. (2012). The age and magma source of Yilvshan granite intrusion are quoted from S. K. Sun et al. (2012) and Nie et al. (2017). The age of Qinshankou granite intrusion is quoted from Luo et al. (2001). The magma source of Qinshankou granite intrusion is quoted from Song (2011). The age of Yu'erya granite intrusion is quoted from T. Zhang et al. (2020). The magma source of Yu'erya granite intrusion is quoted from Kang et al. (1998).

Geochemistry, Geophysics, Geosystems

10.1029/2022GC010769

Table 4
Information, Hg Concentration, and Hg Isotopic Composition of Basement Rock Samples

Sample ID	Stratigraphy	Location	Lithology	THg (ppb)	δ^{202}Hg (‰)	Δ^{199}Hg (‰)	Δ^{200}Hg (‰)	Δ^{201}Hg (‰)
Jiapigou 01	The Paleoproterozoic Ji'an group	128°09′35″, 42°40′20″	Amphibolite	2.95	−0.29	−0.18	−0.07	−0.03
Jiapigou 02		128°07′27″, 42°40′47″	Magnetitic quartzite	23.6	−0.48	−0.04	−0.04	0.01
Jiapigou 03	The Mesoproterozoic Seluohe group	128°04′38″, 42°43′27″	Amphibolite	4.32	−1.03	−0.26	−0.08	−0.19
Jiapigou 04	The Paleoproterozoic Ji'an group	128°08′08″, 42°38′51″	Amphibolite	1.96	−0.63	−0.27	−0.14	−0.14
Jiapigou 05		128°08′49″, 42°38′33″	Amphibolite	10.9	−1.08	−0.11	−0.04	−0.02
Jiapigou 06		128°10′07″, 42°36′53″	Mica schist	7.41	−1.63	−0.02	0.01	0.04
Jiapigou 07	The Neoarchean TTG	Mining area	Monzogranitic gneiss	13.8	−1.37	0.11	−0.02	0.11
Jiapigou 08		127°29′25″, 42°52′03″	Granodioritic gneiss	1.00	−0.92	0.06	−0.08	0.02
Jiapigou 09		Mining area	K-feldspar granitic granulite	0.88	0.07	0.07	−0.03	0.09
Jiapigou 10	The Neoarchean Jiapigou group	Mining area	Migmatited amphibolitic gneiss	2.27	−0.34	−0.30	0.03	−0.26
Jiapigou 11	The Neoarchean TTG	Mining area	Granodioritic gneiss	2.00	0.42	−0.03	−0.05	−0.06
Jiapigou 12		Mining area	Monzogranitic granulite	1.70	0.65	−0.11	−0.03	−0.01
Jiapigou 13		Mining area	Amphibolitic gneiss	15.6	0.55	0.10	0.08	0.03
Jiapigou 14		127°21′20″, 42°54′23″	Granodioritc gneiss	0.91	0.41	−0.09	−0.02	−0.05
Jiapigou 15		127°18′51″, 42°54′24″	Biotite monzogranitc gneiss	1.25	−0.29	−0.09	0.01	−0.04
Jiapigou 16		127°19′56″, 42°55′58″	Granodioritic gneiss	2.61	−0.46	−0.10	0.00	−0.03
Jiapigou 17		127°17′22″, 42°57′24″	Granodioritc gneiss	0.75	−0.03	0.02	−0.08	−0.02
Jiapigou 18		127°16′47″, 42°55′35″	Granodioritc gneiss	2.84	0.60	−0.06	0.00	−0.03
Jinchanggouliang 01	The Xiaotazigou formation of the Neoarchean Jianping group	120°18′53″, 41°58′10″	leptite	11.5	0.05	−0.03	0.00	0.09
Jinchanggouliang 02		120°18′44″, 41°58′01″	Amphibolitic gneiss	2.77	−0.06	−0.37	−0.10	−0.25
Jinchanggouliang 03		120°18′28″, 41°57′58″	Amphibolitic gneiss	2.00	−0.43	0.02	0.02	0.08
Jinchanggouliang 04		120°18′50″, 41°58′03″	Amphibolitic gneiss	3.38	−0.14	0.03	0.08	−0.05
Jinchanggouliang 05		120°17′42″, 41°58′03″	Amphibolitic gneiss	4.46	−0.54	−0.03	0.07	−0.04
Paishanlou 01	The Dayingzi formation of the Neoarchean Jianping group	121°45′58″, 41°46′13″	Amphibolitic gneiss	1.54	−0.48	−0.11	−0.09	0.03
Paishanlou 02		121°46′00″, 41°46′12″	Amphibolitic gneiss	1.85	−0.11	−0.17	−0.04	−0.10
Paishanlou 03		121°47′44″, 41°44′18″	Migmatited amphibolitic gneiss	3.38	0.29	−0.23	−0.04	−0.16
Jinchangyu 01	The Shangchuan formation of the Paleoarchean Qianxi group	118°27′02″, 40°17′19″	Migmatitic granulite	0.62	−0.59	0.00	0.08	−0.04
Jinchangyu 02		118°28′45″, 40°17′44″	Amphibolitic gneiss	0.46	−1.49	−0.17	−0.19	−0.08
Jinchangyu 03		118°30′40″, 40°16′45″	Banded magnetitic quartzite	1.38	−0.27	−0.18	0.12	−0.09
Jinchangyu 04		118°30′48″, 40°15′08″	Migmatitic granulite	1.08	−0.08	−0.21	0.07	−0.16
Jinchangyu 05		118°32′55″, 40°45′37″	Potassic pyroxene granulite	0.77	−0.13	−0.17	0.05	−0.16
Jinchangyu 06		Mining area	Garnet-pyroxene granulite	1.79	−1.20	0.04	0.00	−0.01

Note. The isotope data of sample Jiapigou 04 and Jiapigou 10 are from Deng, Hong, et al. (2022).

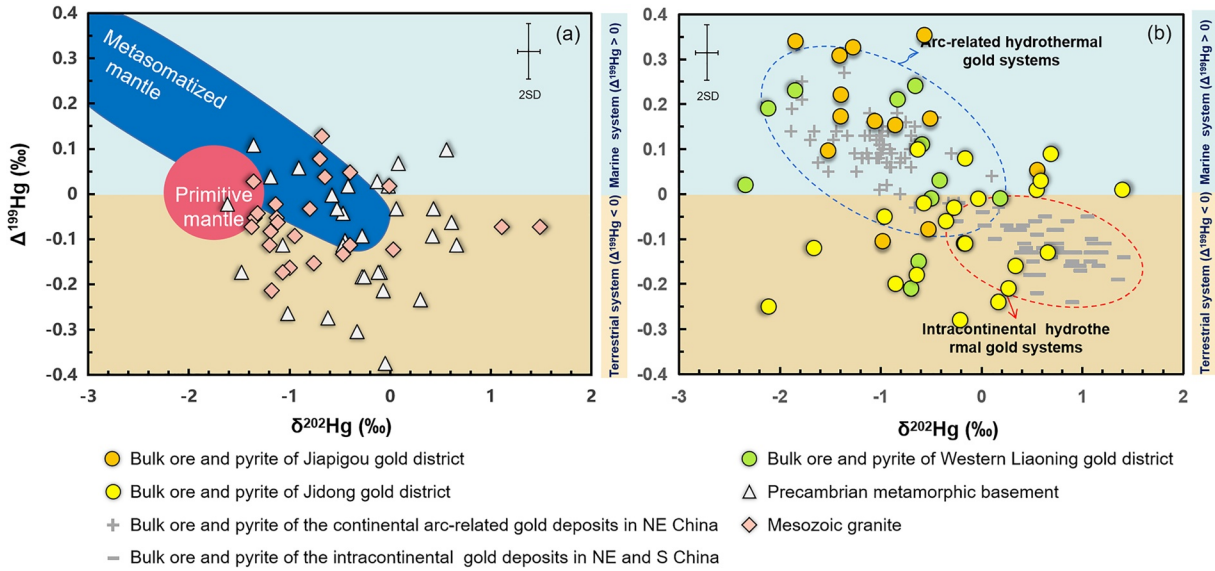

Figure 3. δ^{202}Hg versus Δ^{199}Hg diagrams for the samples of (a) Precambrian metamorphic basement and Mesozoic granite and (b) bulk ore and pyrite of the northern North China Craton in Jiapigou, Jidong, and Western Liaoning gold districts. The pink circle area represents the primitive mantle (Moynier et al., 2021); the dark blue area represents the metasomatized mantle (X. Y. Wang et al., 2021). The results of intracontinental gold deposits are from Deng, Lehmann, et al. (2022), and the results of continental arc-related gold deposits are from Deng et al. (2021).

bulk ore and pyrite samples show elevated Hg concentrations ranging from 0.89 to 221 and 1.52 to 1,230 ppb, with mean values of 23.1 ± 91.0 (n = 25, 2SD) and 87.6 ± 466 ppb (n = 26, 2SD), respectively (Table 2). No independent Hg mineral was observed in any of the samples. Like that observed in other gold deposits (Rytuba, 2003), it is believed that Hg is present mainly as Hg(II) in substitution to Fe(II) in sulfides of the samples investigated, due to their similar ionic radius. Compared with the results of arc-related and intracontinental gold deposits (Deng, Lehmann, et al., 2022), the Hg concentration of gold deposits in NNCC is 2–3 orders of magnitude lower (Figures 5a–5c). This could be due to the fact that NNCC gold deposits were formed at relatively higher temperatures (Table 1), which favor the loss of Hg from the hydrothermal fluids (Smith et al., 2005).

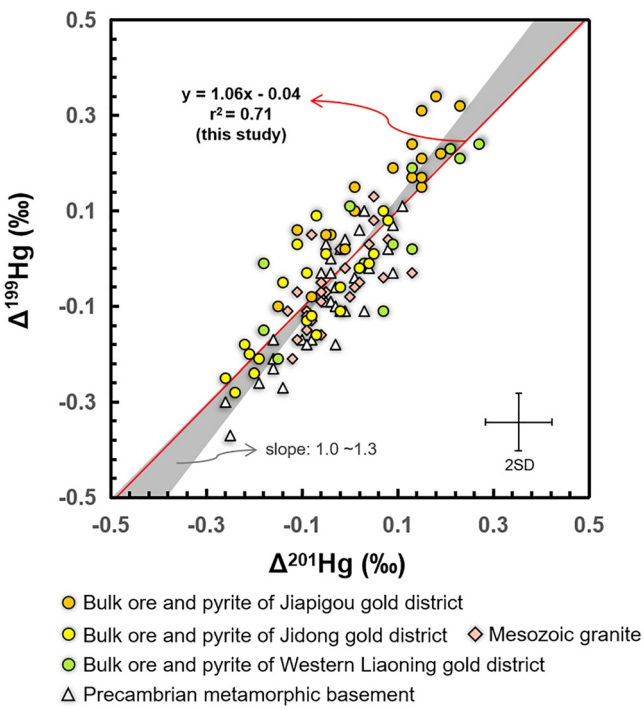

Figure 4. Δ^{201}Hg versus Δ^{199}Hg diagram for the samples investigated in this study.

Precambrian metamorphic basement and granite studied here show δ^{202}Hg ranging from −1.63‰ to 0.65‰ and −1.39‰ to 1.48‰, respectively (Tables 3 and 4 and Figure 3a). Samples of bulk ore and pyrite show a larger δ^{202}Hg range of −3.22‰ to 1.39‰ (Table 2 and Figure 3b). Precambrian metamorphic basement and granite samples show Δ^{199}Hg values ranging from −0.37‰ to 0.11‰ and −0.21‰ to 0.13‰, respectively (Tables 3 and 4 and Figure 3a). The samples of gold ore and pyrite show Δ^{199}Hg ranging from −0.28‰ to 0.34‰ (Table 2 and Figure 3b). All the samples studied show a linear correlation between Δ^{199}Hg and Δ^{201}Hg (Figure 4), with a Δ^{199}Hg/Δ^{201}Hg ratio of 1.06 ± 0.13 (2SD), consistent with that observed during Hg(II) photochemical reduction on Earth's surface (Δ^{199}Hg/Δ^{201}Hg = 1.0 to 1.3; Bergquist & Blum, 2007; Zheng & Hintelmann, 2009) and in basalts and granites (Δ^{199}Hg/Δ^{201}Hg ∼ 1; Deng, Gou, et al., 2022; Moynier et al., 2020, 2021; Tian et al., 2022; X. Y. Wang et al., 2021; Yin et al., 2022).

5. Discussion

5.1. Precambrian Basement as a Major Hg Source for Mesozoic Granites

Large variations of δ^{202}Hg can be observed for the studied granite samples and basement rocks (Figure 3a). The variation of δ^{202}Hg is resulted from

MDF during a large number of processes and cannot provide enough information on Hg sources. A large variation of δ^{202}Hg (~4‰) due to Hg-MDF during hydrothermal processes (e.g., hydrothermal boiling and redox reaction) has been previously reported in epithermal Hg deposits in the USA (Smith et al., 2005, 2008). However, hydrothermal processes are unlikely to produce Hg-MIF (Sherman et al., 2009; Smith et al., 2005, 2008). It is also reported that metamorphic processes could trigger Hg-MDF but do not produce obvious Hg-MIF (Chen et al., 2022; Deng, Hong, et al., 2022; Moynier et al., 2021). Hg-MIF is commonly found in surface reservoirs and is mainly produced via photochemical processes (Blum et al., 2014). The lack of Hg-MIF during geological processes allows the use of Δ^{199}Hg to trace surface Hg recycling into Earth's interior reservoirs (e.g., mantle and crust).

Hg-MIF mainly occurs during Hg photochemical reactions on Earth's surface with no interference from other processes (Yin et al., 2022). The Δ^{199}Hg/Δ^{201}Hg ratio of 1.06 ± 0.13 (2SD) agrees well with that observed for Hg(II) photoreduction (Δ^{199}Hg/Δ^{201}Hg = 1.0 to 1.3; Bergquist & Blum, 2007; Zheng & Hintelmann, 2009), suggesting that a significant fraction of Hg in these samples was ultimately sourced from surface systems. The Δ^{199}Hg values of Mesozoic granite samples (the Jiapigou gold district: −0.07‰ to 0.13‰; the Western Liaoning gold district: −0.21‰ to 0.02‰; and the Jidong gold district: −0.17‰ to 0.05‰) fall in the range for the basement rocks (the Jiapigou gold district: −0.30‰ to 0.11‰; the Western Liaoning gold district: −0.37‰ to 0.03‰; the Jidong gold district: −0.21‰ to 0.04‰) (Tables 3 and 4, Figure 3a). As Mesozoic granites studied here are intruded into the Precambrian basement (Figure 2), inheriting of Hg from partial melting of the Precambrian basement by granites may explain the congruency of Δ^{199}Hg values of the studied basement rocks and granites. This is supported by previous studies based on multiple geochemical indicators that (e.g., REE, trace element, Hf and Pb isotopes) suggest that Mesozoic granites in NNCC were derived from Precambrian basement melting in the lower crust (Fu et al., 2012; Han et al., 2022; Kang et al., 1998; Lu et al., 2019; Song, 2011; S. K. Sun et al., 2012).

5.2. Dual Hg Sources for the NNCC Gold Deposits

The formation of the Mesozoic gold deposits of the NNCC was interpreted as related to either magmatic-hydrothermal (N'dri et al., 2021; Yang et al., 2021) or metamorphic-fluid models (Goldfarb & Pitcairn, 2022; Goldfarb et al., 2001, 2019; Tomkins, 2010), which would suggest that Hg was sourced from the Mesozoic granites or the Precambrian metamorphic basement, respectively. As shown in Figure 3b, bulk ore and pyrite samples show Δ^{199}Hg values of −0.28‰ to 0.34‰, which cover a larger range than that of the Mesozoic granites (−0.21‰ to 0.13‰) and the Precambrian basement rocks (−0.37‰ to 0.11‰), suggesting that the gold deposits studied cannot be explained exclusively by any of the above-mentioned models. Instead, we suggest that the sources of Hg (and Au, by analogy) are variable among different gold deposits, as discussed below.

The two Middle Jurassic (~160 Ma) gold deposits (Jiapigou and Songjianghe) in the Jiapigou gold district mainly show positive Δ^{199}Hg values with a mean of 0.14‰ ± 0.26‰ (n = 18, 2SD) (Figure 5a). The Jiapigou gold district was located in an active continental arc in the Jurassic and formed during the subduction of the paleo-Pacific plate at ~160 Ma. The lithospheric mantle is greatly modified by fluid released from the subducted oceanic plate during this stage (F. Guo et al., 2015). The mostly positive Δ^{199}Hg values of the Jiapigou gold district (−0.1‰ to 0.34‰) are consistent with those observed in ocean sediments and metasomatized mantle materials (Δ^{199}Hg: −0.08‰ to 0.37‰; X. Y. Wang et al., 2021) rather than Precambrian basement rocks in the area (Δ^{199}Hg: −0.30 to 0.11; This study). In addition, as shown in Figure 5a, the Δ^{199}Hg values of the Jiapigou gold district almost overlap with those of arc-related epithermal gold systems, suggesting that Hg was derived from a marine source via oceanic plate subduction (Deng et al., 2021). We hereby suggest that the gold deposits of Jiapigou district should have received predominantly ocean-recycled Hg from the subducted paleo-Pacific slab.

Contrary to the Jiapigou gold district, the two ~160 Ma gold deposits (Jinchangyu and Yu'erya) in the Jidong district mainly show negative Δ^{199}Hg values with a mean value of −0.07‰ ± 0.24‰ (n = 19, 2SD) (Figure 5b). The predominantly negative Δ^{199}Hg values in the Jinchangyu gold district are consistent with that observed for the Precambrian basement rocks in the area (Δ^{199}Hg: −0.21‰ to 0.04‰). Previous studies on intracontinental Au deposits in SW China and NE China also observed negative Δ^{199}Hg values (Δ^{199}Hg: −0.24‰ to −0.02‰; Figure 5b), which were attributed to the addition of mobilized Hg from the Precambrian basement (Deng, Lehmann, et al., 2022). The Δ^{199}Hg values of Jidong gold deposits mostly overlap with those of intracontinental Au deposits (Deng, Lehmann, et al., 2022). Therefore, we suggest the Precambrian metamorphic basement is the

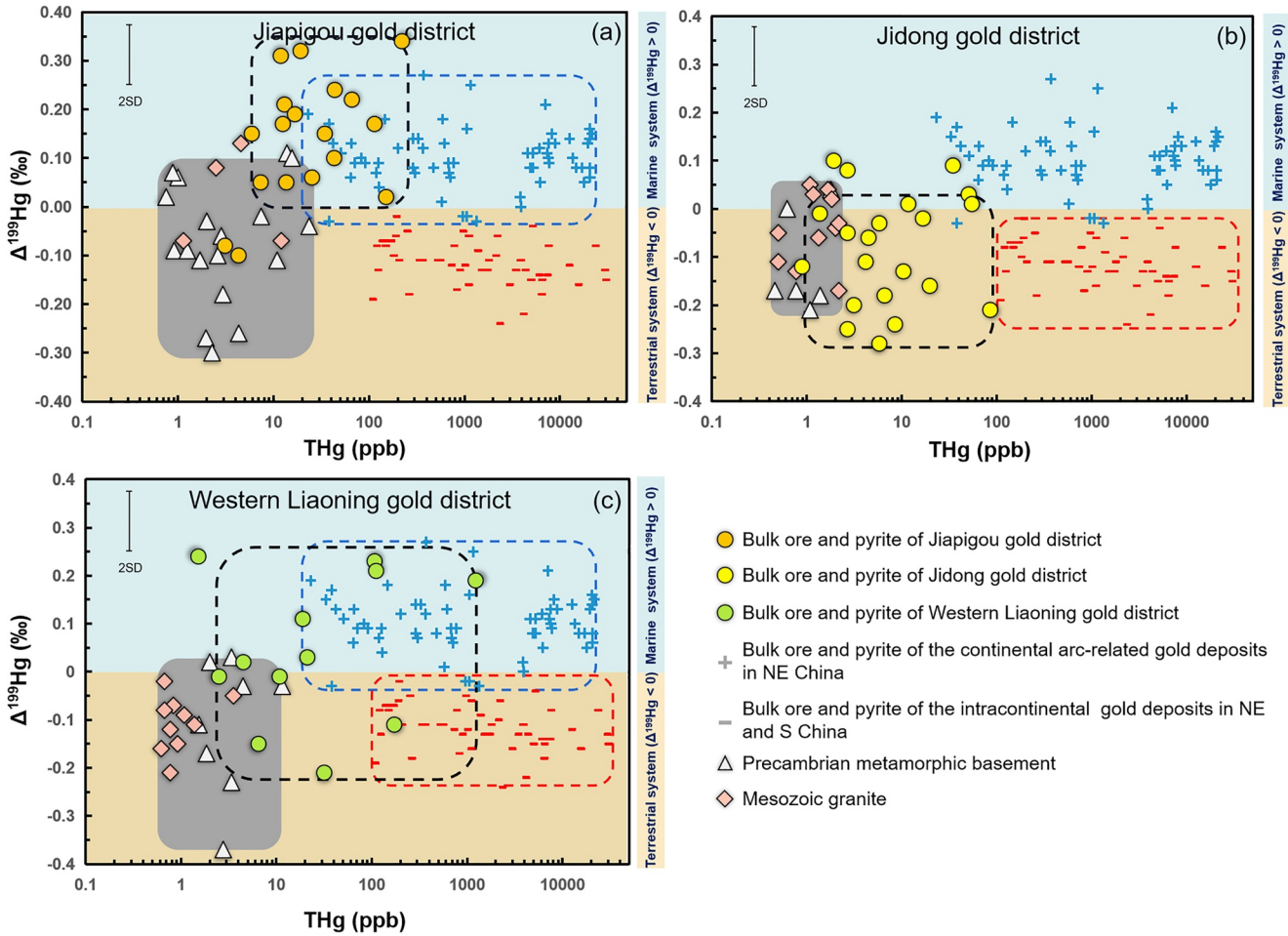

Figure 5. THg versus Δ^{199}Hg diagram for the samples investigated in this study.

most probable Hg source for the Jidong gold deposits. This is supported by the fact that the Jidong gold district is located on the inner continent behind the active continental arc (Yang et al., 2021 and references therein), with the lack of significant influence from the subducted paleo-Pacific plate.

Both positive and negative Δ^{199}Hg values with a mean of 0.01‰ ± 0.32‰ (n = 14, 2SD) were observed in the ~130 Ma gold deposits (Paishanlou and Jinchanggouliang) in the Western Liaoning gold district (Figure 5c). The Precambrian basement rocks and Mesozoic granites in this area show negative Δ^{199}Hg values. The negative Δ^{199}Hg values in some of these gold deposits may be explained by the contribution of Hg from the Precambrian basement, similar to the Jidong gold district. Meanwhile, the Western Liaoning gold district was formed during the destruction of the NCC destruction at ~130 Ma (Zhu & Sun, 2021). Prior to 130 Ma, the lithospheric mantle beneath the NCC had been extensively metasomatized by fluids released by the subducted oceanic slab (Zhu & Sun, 2021). Therefore, the positive Δ^{199}Hg values observed in the Paishanlou and Jinchanggouliang deposits suggest that some Hg is also sourced from the metasomatized lithosphere mantle. The occurrence of both positive and negative Δ^{199}Hg values in the Western Liaoning gold district indicates binary mixing of ocean-recycled Hg (from the subducted paleo-Pacific slab) and terrestrial-recycled Hg (from the Precambrian basement) with opposing Δ^{199}Hg signals. We infer that fluids both from the subducted oceanic slab and continental basement contributed Hg to the ~130 Ma gold deposits in the Western Liaoning gold district.

5.3. Genetic Model for the Mesozoic Gold Deposits in the NNCC

Results of this study allow us to develop a genetic model for the Mesozoic gold deposits in the NNCC (Figure 6). During the Middle-Late Mesozoic, two major stages of magmatism occurred in the NNCC at ~160 and ~130 Ma,

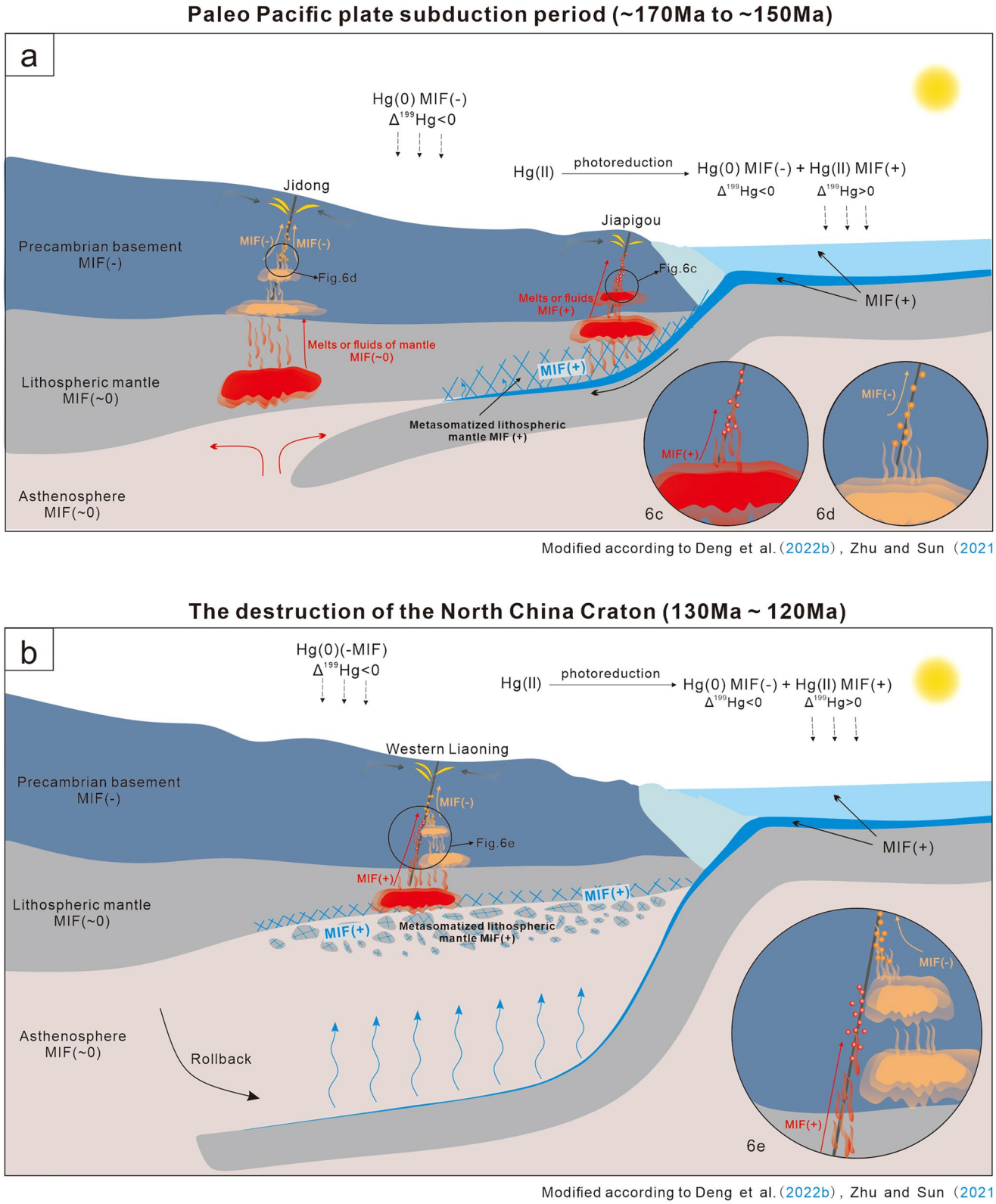

Figure 6. Genetic model showing potential scenarios for gold mineralization due to (a) subduction of the paleo-Pacific plate in 170–150 Ma period and (b) due to NNC destruction at ~130 Ma.

respectively (Yang et al., 2003, 2008; Zhu & Sun, 2021). Subduction of the paleo-Pacific plate is believed to be responsible for the magmatism occurring at ~160 Ma (Yang et al., 2003, 2008; Zhu & Sun, 2021; Figure 6a), whereas the rollback of the paleo-Pacific plate associated with deep and steep subduction is proposed as the cause of NCC destruction that occurred at ~130 Ma (Zhu and Sun., 2021; Figure 6b). During the Jurassic, the Jiapigou area was located in the active continental arc, and the involvement of subducted oceanic slab could contribute abundant marine-derived volatiles and fluids (e.g., H_2O, CO_2, and Hg) into the lithospheric mantle, causing positive Δ^{199}Hg values of the lithospheric mantle and inducing arc magmatism as well. During this process, the ascension of mantle-derived magmas and hydrothermal solutions into the upper crust could have released sufficient amounts of fluids containing recycled marine Hg, favoring the formation of gold deposits in the Jiapigou gold district with positive Δ^{199}Hg values (Figure 6c). The negative Δ^{199}Hg values in the Jidong gold district, which was located in a relatively intercontinental environment, could be formed by fluid released from the remobilized Precambrian basement due to heat flow and crustal compression thickening driven by paleo-Pacific plate subduction (Figure 6d).

Since the Early Cretaceous, the rollback of the paleo-Pacific plate triggered the destruction of the NCC, as represented by lithospheric thinning and upwelling of the asthenosphere (Zhu & Sun, 2021). Destruction of the NCC not only drove the melting of the metasomatized mantle to release magmatic-hydrothermal fluids characterized by positive Δ^{199}Hg values but also could benefit remobilization of the Precambrian basement to release ore-forming fluids containing Hg with negative Δ^{199}Hg values (Figure 6e). These two kinds of fluids favored the formation of the ~130 Ma gold deposits in the Western Liaoning gold district, which could explain the existence of both positive and negative Δ^{199}Hg in these deposits.

The distinct Hg-MIF signals between the Jiapigou gold district (mostly positive Δ^{199}Hg values) and Jidong gold district (mostly negative Δ^{199}Hg values) may be related to their distinct tectonic environment. Combined with the Δ^{199}Hg characteristics and tectonic evolution of the three regions, whether positive MIF signals occur in gold deposits depends on the amount of subducted oceanic plate-derived fluids that affected the lithosphere. In analogy to Hg, the source of gold lies both in the metasomatized lithospheric mantle (positive Δ^{199}Hg) and the continental basement (negative Δ^{199}Hg), with variable contributions from both reservoirs depending on the regional geotectonic situation or, ultimately, the translithospheric heat flow driven by subducting oceanic plate.

6. Conclusion

In summary, our results on Hg isotopes show that the source of ore-forming materials of the Mesozoic gold deposits in the NNCC can be both Precambrian metamorphic basement and lithospheric mantle metasomatized by subduction oceanic plates. Mesozoic gold deposits show variable Δ^{199}Hg values. Gold deposits with negative Δ^{199}Hg receive Hg mainly from the Precambrian metamorphic basement, while those with positive Δ^{199}Hg receive Hg from the lithospheric mantle metasomatized by the subducted paleo-Pacific slab. This study shows a novel application of Hg isotopes as a source tracer for hydrothermal gold deposits and highlights their potential for metallogenetic tracing in other hydrothermal systems.

Data Availability Statement

The data set of this research (Yin, 2022) can be found in a public domain repository.

Acknowledgments
This work was supported by the National Natural Science Foundation of China (41873047). Professor Richard Goldfarb from the Colorado School of Mines is thanked for providing insightful suggestions.

References

Bergquist, B. A., & Blum, J. D. (2007). Mass-dependent and -independent fractionation of Hg isotopes by photoreduction in aquatic systems. *Science*, *318*(5849), 417–420. https://doi.org/10.1126/science.1148050

Blum, J. D., Sherman, L. S., & Johnson, M. W. (2014). Mercury isotopes in Earth and environmental sciences. *Annual Review of Earth and Planetary Sciences*, *42*(1), 249–269. https://doi.org/10.1146/annurev-earth-050212-124107

Chen, D., Ren, D. S., Deng, C. Z., Tian, Z. D., & Yin, R. S. (2022). Mercury loss and isotope fractionation during high-pressure and high-temperature processing of sediments: Implication for the behaviors of mercury during metamorphism. *Geochimica et Cosmochimica Acta*, *334*, 231–240. https://doi.org/10.1016/j.gca.2022.08.010

Dai, Z. J., Wang, K. Y., & Cheng, X. M. (2007). Geochemical features of ore-forming fluids in the Jiapigou Gold Belt, Jinlin Province. *Acta Petrologica Sinica*, *23*(375), 2198–2206.

Deng, C. Z., Gou, J., Sun, D. Y., Sun, G. Y., Tian, Z. D., Lehmann, B., et al. (2022). Mercury isotopic composition of igneous rocks from an accretionary orogen: Implications for lithospheric recycling. *Geology*, *50*(9), 1001–1006. https://doi.org/10.1130/g50131.1

Deng, C. Z., Hong, Y. G., Xiao, T. T., Chen, D., Sun, G. Y., & Yin, R. S. (2022). Mercury isotopic compositions of the Precambrian rocks and implications for tracing mercury cycling in Earth's interior. *Precambrian Research*, *373*, 106646. https://doi.org/10.1016/j.precamres.2022.106646

Deng, C. Z., Lehmann, B., Xiao, T. T., Tan, Q. P., Chen, D., Tian, Z. D., et al. (2022). Intracontinental and arc-related hydrothermal systems display distinct δ^{202}Hg and Δ^{199}Hg features: Implication for large-scale mercury recycling and isotopic fractionation in different tectonic settings. *Earth and Planetary Science Letters*, *593*, 117646. https://doi.org/10.1016/j.epsl.2022.117646

Deng, C. Z., Sun, G. Y., Rong, Y. M., Sun, R. Y., Sun, D. Y., Lehmann, B., & Yin, R. S. (2021). Recycling of mercury from the atmosphere-ocean system into volcanic-arc-associated epithermal gold systems. *Geology*, *49*(3), 309–313. https://doi.org/10.1130/g48132.1

Fu, L. B., Wei, J. H., Kusky, T. M., Chen, H. Y., Tan, J., Li, Y. J., et al. (2012). The Cretaceous Duimiangou adakite-like intrusion from the Chifeng region, northern North China Craton: Crustal contamination of basaltic magma in an intracontinental extensional environment. *Lithos*, *134–135*, 273–288. https://doi.org/10.1016/j.lithos.2012.01.007

Goldfarb, R. J., Groves, D. I., & Gardoll, S. (2001). Orogenic gold and geologic time: A global synthesis. *Ore Geology Reviews*, *18*(1–2), 1–75. https://doi.org/10.1016/s0169-1368(01)00016-6

Goldfarb, R. J., & Pitcairn, I. (2022). Orogenic gold: Is a genetic association with magmatism realistic? *Mineralium Deposita*, *58*(1), 5–35. https://doi.org/10.1007/s00126-022-01146-8

Goldfarb, R. J., Qiu, K. F., Deng, J., Chen, Y. J., & Yang, L. Q. (2019). Orogenic gold deposits of China. *Society of Economic Geologists*, *22*, 263–324.

Guo, B. W., Xu, Y. X., Li, l.X., Guo, Z. H., Hu, B., & Wang, S. Z. (2017). The significance and characteristics of inclusions of Yu'erya gold deposit in eastern Hebei Province. *China Mining Magazine*, *26*, 237–240.

Guo, F., Li, H. X., Fan, W. M., Li, J. Y., Zhao, L., Huang, M. W., & Xu, W. L. (2015). Early Jurassic subduction of the Paleo-Pacific Ocean in NE China: Petrologic and geochemical evidence from the Tumen mafic intrusive complex. *Lithos*, *224–225*, 46–60. https://doi.org/10.1016/j.lithos.2015.02.014

Han, J. L., Deng, J., Zhang, Y., Sun, J. G., Wang, Q. F., Zhang, Y. M., et al. (2022). Au mineralization-related magmatism in the giant Jiapigou mining district of Northeast China. *Ore Geology Reviews*, *141*, 104638. https://doi.org/10.1016/j.oregeorev.2021.104638

Jia, S. S. (2011). *Dynamical mechanisms of gold metallogenic localization and metallogenic prediction in Eastern Hebei-Western Liaoning. Shengyang China* (pp. 59–61). Northeastern University.

Kang, X. G., Yang, R. Y., Chen, K. R., & Chen, X. M. (1998). Petrology characteristics of granites in Yu'erya mine of Hebei. *Acta Scientiarum Naturalium Universitatis Sunyatseni*, *37*, 103–107.

Kong, D. X., Xu, J. F., Yin, J. W., Chen, J. L., Li, J., Guo, Y., et al. (2015). Electron microprobe analyses of ore minerals and H-O, S isotope geochemistry of the Yuerya gold deposit, eastern Hebei, China: Implications for ore Genesis and mineralization. *Ore Geology Reviews*, *69*, 199–216. https://doi.org/10.1016/j.oregeorev.2015.01.020

Li, J. W., Bi, S. J., Selby, D., Chen, L., Vasconcelos, P., Thiede, D., et al. (2012). Giant Mesozoic gold provinces related to the destruction of the North China craton. *Earth and Planetary Science Letters*, *349–350*, 26–37. https://doi.org/10.1016/j.epsl.2012.06.058

Liu, L., Gu, X. X., Zhang, Y. M., Ouyang, X., Wang, L. Z., & Gao, L. Y. (2020). Genesis of the Jinchanggouliang gold deposit, Chifeng, China: Constraints from fluid inclusions and isotopic geochemistry. *Ore Geology Reviews*, *115*, 103180. https://doi.org/10.1016/j.oregeorev.2019.103180

Liu, S. F., Wang, Q. F., Groves, D. I., Wang, Z. M., Yang, L., Wu, Z. L., et al. (2021). Adoption of a mineral system model in successful deep exploration at Erdaogou, China's deepest gold mine, on the northeastern margin of the North China Craton. *Ore Geology Reviews*, *131*, 104060. https://doi.org/10.1016/j.oregeorev.2021.104060

Lu, Q., Sun, J. G., An, Z. H., Han, J. L., & Chu, X. L. (2019). Petrogenesis and forming environment of Mesozoic porphyritic granite in Songjianghe region of Dunhua, Jinlin Province: Evidences from element geochemistry, Hf isotope and U-Pb. *Journal of Jilin University (Earth Science Edition)*, *49*, 673–685.

Luo, Z. K., Guan, K., Qiu, Y. S., Miao, L. C., Qiu, Y. M., J, M. N., & Groves, D. I. (2001). Zircon shrimp U-Pb dating of albite dyke in Jinchangyu gold mine, Jidong area, Hebei, China. *Contributions to Geology and Mineral Resources Research*, *16*, 226–231.

Mo, L. C., Liu, F. L., Zhang, C. Z., He, S., Li, D., Chang, L. G., & Yang, Z. M. (2021). Mineralization timing and geodynamic background of the Jinchanggouliang gold deposit in Inner Mongolia. *Acta Petrologica Sinica*, *37*(6), 1799–1812. https://doi.org/10.18654/1000-0569/2021.06.10

Moynier, F., Chen, J. B., Zhang, K., Cai, H. M., Wang, Z. C., Jackson, M. G., & Day, J. M. D. (2020). Chondritic mercury isotopic composition of Earth and evidence for evaporative equilibrium degassing during the formation of eucrites. *Earth and Planetary Science Letters*, *551*, 116544. https://doi.org/10.1016/j.epsl.2020.116544

Moynier, F., Jackson, M. G., Zhang, K., Cai, H. M., Halldórsson, S. A., Pik, R., et al. (2021). The mercury isotopic composition of Earth's mantle and the use of mass independently fractionated Hg to test for recycled crust. *Geophysical Research Letters*, *48*(17), e2021GL094301. https://doi.org/10.1029/2021gl094301

N'dri, K. A., Zhang, D. H., Zhang, T., Tamehe, L. S., Kouamelan, K. S., Wu, M. Q., et al. (2021). Gold mineralization in the northern margin of the North China Craton: Influence of alkaline magmatism and regional tectonic during Middle Paleozoic-Mesozoic. *Ore Geology Reviews*, *133*, 103969. https://doi.org/10.1016/j.oregeorev.2020.103969

Nie, S. J., Yang, Y. C., Zhang, L., & Wang, F. B. (2017). Formation age and geological significance of biotite granite in Paishanlou Au deposit of Liaoning, China. *Journal of Earth Sciences and Environment*, *39*, 161–174.

Qin, Z., Sun, D. Y., Zhang, J. L., Li, L. W., Wang, Z. Y., & Li, X. J. (2019). Characteristics of fluid inclusions and metallogenic physicochemical conditions of Songjianghe gold deposit in Dunhua, Jilin province. *Gold*, *40*, 14–18.

Rytuba, J. J. (2003). Mercury from mineral deposits and potential environmental impact. *Environmental Geology*, *43*(3), 326–338. https://doi.org/10.1007/s00254-002-0629-5

Sherman, L. S., Blum, J. D., Nordstrom, D. K., McCleskey, R. B., Barkay, T., & Vetriani, C. (2009). Mercury isotopic composition of hydrothermal systems in the Yellowstone Plateau volcanic field and Guaymas Basin sea-floor rift. *Earth and Planetary Science Letters*, *279*(1–2), 86–96. https://doi.org/10.1016/j.epsl.2008.12.032

Smith, C. N., Kesler, S. E., Blum, J. D., & Rytuba, J. J. (2008). Isotope geochemistry of mercury in source rocks, mineral deposits and spring deposits of the California Coast Ranges, USA. *Earth and Planetary Science Letters*, *269*(3–4), 399–407. https://doi.org/10.1016/j.epsl.2008.02.029

Smith, C. N., Kesler, S. E., Klaue, B., & Blum, J. D. (2005). Mercury isotope fractionation in fossil hydrothermal systems. *Geology*, *33*(10), 825–828. https://doi.org/10.1130/g21863.1

Song, Y. (2011). *Study for the tectono-magmatic function and fluid metallogenic process of typical gold deposits in Jidong region* (pp. 80–82). China University of Geosciences.

Song, Y., Jiang, S. H., Bagas, L., Li, C., Hu, J. Z., Zhang, Q., et al. (2016). The geology and geochemistry of Jinchangyu gold deposit, North China Craton: Implications for metallogenesis and geodynamic setting. *Ore Geology Reviews*, *73*, 313–329. https://doi.org/10.1016/j.oregeorev.2014.10.031

Sun, S. K., Liu, H. T., & Chu, S. X. (2012). Origin of the Paishanlou monzogranite in Liaoning Province and its genetic connection with gold mineralization. *Acta Petrologica Sinica*, *28*, 607–618.

Sun, Z. J., Li, X. Y., Yu, H. N., Sun, G. S., Zhu, J. H., Lu, L. N., & Su, R. (2014). Characteristics of ore-forming fluid and stable isotope from Jingchanggouliang gold deposit in Inner Mongolia. *Global Geology*, *33*, 591–490.

Tian, Z. D., Leng, C. B., Deng, C. Z., Zhang, X. C., Chen, D., Gao, L. J., et al. (2022). Mercury isotopes as a useful tracer of magma sources: An example from the Daocheng-Cuojiaoma batholith, eastern Tibetan Plateau. *Chemical Geology*, *606*, 120974. https://doi.org/10.1016/j.chemgeo.2022.120974

Tomkins, A. G. (2010). Windows of metamorphic sulfur liberation in the crust: Implications for gold deposit Genesis. *Geochimica et Cosmochimica Acta*, *74*(11), 3246–3259. https://doi.org/10.1016/j.gca.2010.03.003

Wang, H. Q., Gao, W. S., Deng, X. D., & Li, J. W. (2020). Zircon U-Pb dating reveals Late Jurassic gold mineralization in the Jidong district of the northern North China Craton. *Ore Geology Reviews*, *126*, 103798. https://doi.org/10.1016/j.oregeorev.2020.103798

Wang, X. Y., Deng, C. Z., Yang, Z. Y., Zhu, J. J., & Yin, R. S. (2021). Oceanic mercury recycled into the mantle: Evidence from positive Δ^{199}Hg in lamprophyres. *Chemical Geology*, *584*, 120505. https://doi.org/10.1016/j.chemgeo.2021.120505

Yang, J. H., Wu, F. Y., & Wilde, S. A. (2003). A review of the geodynamic setting of large-scale late mesozoic gold mineralization in the North China Craton: An association with lithospheric thinning. *Ore Geology Reviews*, *23*(3–4), 125–152. https://doi.org/10.1016/s0169-1368(03)00033-7

Yang, J. H., Wu, F. Y., Wilde, S. A., Belousova, E., & Griffin, W. L. (2008). Mesozoic decratonization of the North China block. *Geology*, *36*(6), 467–470. https://doi.org/10.1130/g24518a.1

Yang, J. H., Xu, L., Sun, J. F., Zeng, Q. D., Zhao, Y. N., Wang, H., & Zhu, Y. S. (2021). Geodynamics of decratonization and related magmatism and mineralization in the North China Craton. *Science China Earth Sciences*, *64*(9), 1409–1427. https://doi.org/10.1007/s11430-020-9732-6

Yin, R. S. (2022). Dataset for manuscript "Paleo-Pacific plate subduction and basement mobilization triggered large-scale formation of Mesozoic gold deposits in the northern margin of the North China Craton" [Dataset]. Figshare. https://doi.org/10.6084/m9.figshare.21443262.v1

Yin, R. S., Chen, D., Pan, X., Deng, C. Z., Chen, L. M., Song, X. Y., et al. (2022). Mantle Hg isotopic heterogeneity and evidence of oceanic Hg recycling into the mantle. *Nature Communications*, *13*(1), 1–7. https://doi.org/10.1038/s41467-022-28577-1

Yin, R. S., Krabbenhoft, D. P., Bergquist, B. A., Zheng, W., Lepak, R. F., & Hurley, J. P. (2016). Effects of mercury and thallium concentrations on high precision determination of mercury isotopic composition by Neptune Plus multiple collector inductively coupled plasma mass spectrometry. *Journal of Analytical Atomic Spectrometry*, *31*(10), 2060–2068. https://doi.org/10.1039/c6ja00107f

Zerkle, A. L., Yin, R. S., Chen, C. Y., Li, X. D., Izon, G. J., & Grasby, S. E. (2020). Anomalous fractionation of mercury isotopes in the Late Archean atmosphere. *Nature Communications*, *11*(1), 1–9. https://doi.org/10.1038/s41467-020-15495-3

Zhang, S. H., Zhao, Y., Davis, G. A., Ye, H., & Wu, F. (2014). Temporal and spatial variations of Mesozoic magmatism and deformation in the North China Craton: Implications for lithospheric thinning and decratonization. *Earth-Science Reviews*, *131*, 49–87. https://doi.org/10.1016/j.earscirev.2013.12.004

Zhang, T., Zhang, D. H., Danyushevsky, L. V., Wu, M. Q., Koffi Alexis, N. D., Liao, Y. Z., & Zhang, J. L. (2020). Timing of multiple magma events and duration of the hydrothermal system at the Yu'erya gold deposit, eastern Hebei Province, China: Constraints from U-Pb and Ar-Ar dating. *Ore Geology Reviews*, *127*, 103804. https://doi.org/10.1016/j.oregeorev.2020.103804

Zhang, X. H., Liu, Q., Ma, Y. J., & Wang, H. (2005). Geology, fluid inclusions, isotope geochemistry, and geochronology of the Paishanlou shear zone-hosted gold deposit, North China Craton. *Ore Geology Reviews*, *26*(3–4), 325–348. https://doi.org/10.1016/j.oregeorev.2005.03.001

Zhang, X. H., & Zhai, M. G. (2010). Magmatism and its metallogenetic effects during the Paleozoic continental crustal construction in northern North China: An overview. *Acta Petrologica Sinica*, *26*(5), 1329–1341.

Zhang, X. T., Sun, J. G., Han, J. L., & Feng, Y. Y. (2021). Genesis and ore-forming process of the Benqu mesothermal gold deposit in the Jiapigou ore cluster, NE China: Constraints from geology, geochronology, fluid inclusions, and whole- rock and isotope geochemistry. *Ore Geology Reviews*, *130*, 103956. https://doi.org/10.1016/j.oregeorev.2020.103956

Zhang, X. T., Sun, J. G., Yu, Z. T., & Song, Q. H. (2019). LA-ICP-MS zircon U-Pb and sericite ^{40}Ar/^{39}Ar ages of the Songjianghe gold deposit in southeastern Jilin Province, Northeast China, and their geological significance. *Canadian Journal of Earth Sciences*, *56*(6), 607–628. https://doi.org/10.1139/cjes-2018-0254

Zhang, Y. B., Wu, F. Y., Li, H. M., Lu, X. P., Sun, D. Y., & Zhou, H. Y. (2002). Single grain zircon U-Pb ages of the Huangniling granite in Jilin province. *Acta Petrologica Sinica*, *18*, 475–481.

Zhao, G. C., & Zhai, M. G. (2013). Lithotectonic elements of Precambrian basement in the North China Craton: Review and tectonic implications. *Gondwana Research*, *23*(4), 1207–1240. https://doi.org/10.1016/j.gr.2012.08.016

Zheng, W., & Hintelmann, H. (2009). Mercury isotope fractionation during photoreduction in natural water is controlled by its Hg/DOC ratio. *Geochimica et Cosmochimica Acta*, *73*(22), 6704–6715. https://doi.org/10.1016/j.gca.2009.08.016

Zhu, R. S., & Sun, W. D. (2021). The big mantle wedge and decratonic gold deposits. *Science China Earth Sciences*, *64*(9), 1451–1462. https://doi.org/10.1007/s11430-020-9733-1